Published online 10 February 2022 *Nucleic Acids Research, 2022, Vol. 50, No. 4* **2319–2333**
https://doi.org/10.1093/nar/gkab1288

Role of PemI in the *Staphylococcus aureus* PemIK toxin–antitoxin complex: PemI controls PemK by acting as a PemK loop mimic

Do-Hee Kim [1,2,3,†], Sung-Min Kang [4,†], Sung-Min Baek[3], Hye-Jin Yoon[5], Dong Man Jang[6], Hyoun Sook Kim[6], Sang Jae Lee [7,*] and Bong-Jin Lee [3,*]

[1]Jeju Research Institute of Pharmaceutical Sciences, College of Pharmacy, Jeju National University, Jeju 63243, Republic of Korea, [2]Interdisciplinary Graduate Program in Advanced Convergence Technology & Science, Jeju National University, Jeju 63243, Republic of Korea, [3]The Research Institute of Pharmaceutical Sciences, College of Pharmacy, Seoul National University, Seoul 08826, Republic of Korea, [4]College of Pharmacy, Duksung Women's University, Seoul 01369, Republic of Korea, [5]Department of Chemistry, Seoul National University, Seoul 08826, Republic of Korea, [6]Research Institute, National Cancer Center, Goyang, Gyeonggi 10408, Republic of Korea and [7]PAL-XFEL, Pohang Accelerator Laboratory, POSTECH, Pohang, Gyeongbuk 37673, Republic of Korea

Received June 09, 2021; Revised December 15, 2021; Editorial Decision December 15, 2021; Accepted December 17, 2021

ABSTRACT

***Staphylococcus aureus* is a notorious and globally distributed pathogenic bacterium. New strategies to develop novel antibiotics based on intrinsic bacterial toxin–antitoxin (TA) systems have been recently reported. Because TA systems are present only in bacteria and not in humans, these distinctive systems are attractive targets for developing antibiotics with new modes of action. *S. aureus* PemIK is a type II TA system, comprising the toxin protein PemK and the labile antitoxin protein PemI. Here, we determined the crystal structures of both PemK and the PemIK complex, in which PemK is neutralized by PemI. Our biochemical approaches, including fluorescence quenching and polarization assays, identified Glu20, Arg25, Thr48, Thr49, and Arg84 of PemK as being important for RNase function. Our study indicates that the active site and RNA-binding residues of PemK are covered by PemI, leading to unique conformational changes in PemK accompanied by repositioning of the loop between β1 and β2. These changes can interfere with RNA binding by PemK. Overall, PemK adopts particular open and closed forms for precise neutralization by PemI. This structural and functional information on PemIK will contribute to the discovery and development of novel antibiotics in the form of peptides or small molecules inhibiting direct binding between PemI and PemK.**

INTRODUCTION

Toxin-antitoxin (TA) systems are modules that comprise a set of genes encoding a toxin and an antitoxin. The first TA system was discovered in the *Escherichia coli* F plasmid (1). The plasmid addiction module produces a stable antibacterial toxin that impairs an essential cellular process and a labile antitoxin that neutralizes the deleterious activity of the toxin (2). However, in plasmid-free cells, both toxins and antitoxins are not replenished, and the antitoxin is degraded more rapidly by the host enzyme than the toxin. Eventually, the remaining free toxin triggers death or growth arrest of the cell (2,3). Later, it was discovered that many TA systems also exist in bacterial chromosomes, in addition to plasmids. Recently, based on regulatory roles in the virulence and survival of bacteria under stress conditions, TA systems have been considered to be attractive targets for the development of novel antibiotics (4–6).

TA systems have been classified into six types according to the mode of actions and the nature of antitoxins: the proteins are classified as type II, IV, V or VI, whereas the RNAs are classified as type I or III (7). In the type II system, toxins generally exhibit ribonuclease (RNase) activities and are further classified according to ribosomal dependency (8), cellular target (9), and mode of action (9,10).

Although TA systems are widespread among bacteria, *Staphylococcus aureus* carries fewer type II TA system components than other species, such as *Mycobacterium tuberculosis* and *E. coli* (11,12). To date, three kinds of type II TA pairs have been experimentally verified in *S. aureus*, namely, MazEF/PemIK, YefM-YoeB (AxeTxe) and Omega-Epsilon-Zeta (13–15). Among them, MazEF is one

*To whom correspondence should be addressed. Tel: +82 2 880 7869; Email: lbj@nmr.snu.ac.kr
Correspondence may also be addressed to Sang Jae Lee. Tel: +82 54 279 1490; Email: sangjaelee@postech.ac.kr
†The authors wish it to be known that, in their opinion, the first two authors should be regarded as Joint First Authors.

of the extensively characterized TA systems (14). The toxin MazF dimer is an RNase that specifically cleaves the mRNA sequence UACAU in a ribosome-independent manner. It forms the hexameric MazF2–MazE2–MazF2 complex by binding to the antitoxin MazE dimer.

In *S. aureus* CH91, plasmid emergency maintenance inhibitor or killing (PemIK) (16) was discovered as a novel type II TA system (17). The *pemIK* locus is encoded by a 17-kb plasmid (pCH91) of *S. aureus* CH91 that contains genes related to virulence factors and plasmid stability (18,19). The toxin PemK, as an endoribonuclease, specifically recognizes and cleaves the tetrad sequence U↓AUU in a target mRNA in a ribosome-independent manner (20). The antitoxin PemI is hypothesized to perform dual actions of a transcription factor and a neutralizer of toxin activity, which also allows bacterial survival. Interestingly, the target sequence (U↓AUU) of PemK is found in a considerable number of mRNA transcripts encoding proteins involved in virulence but not in the cell translation machinery (17,21–24). Additionally, *S. aureus* PemK affected protein regulation in *Caenorhabditis elegans*, which is a relevant model of higher eukaryotes, according to the research by Mir *et al.* (25). The regulated proteins were involved in ATP generation, protein synthesis, lipid synthesis, cytoskeleton function, heat shock response, innate immune defence, stress response, neuron degeneration, muscle assembly, and so on. Regarding the other pathogenic bacteria, including *Klebsiella pneumonia, Bacillus anthracis* and *Mycobacterium tuberculosis*, overexpression of the *pemK* gene led to the severe inhibition of bacterial growth (26–28). PemK toxins modulate specific gene pools of the bacterial transcriptome in an orchestrated manner but remain elusive at the experimental level (28). Despite these roles of PemIK as a global virulence modulator in *S. aureus*, the structure and function of *S. aureus* PemIK remain unknown.

In this study, we determined the crystal structures of both *S. aureus* PemK and PemI-neutralized PemK. The structures demonstrate an RNase SH3-like fold for PemK and PemI-induced conformational changes in PemK. Biophysical and biochemical analyses with mutagenesis experiments have revealed the key residues for the activity of *S. aureus* PemK. These results provide a structural basis for understanding the molecular function of PemIK and a platform for the discovery of novel antibiotics.

MATERIALS AND METHODS

Gene cloning

The genes encoding PemK and PemI from plasmid pCH91, which was isolated from *S. aureus* CH-91 (29), were synthesized by Bioneer (Daejeon, Korea) and PCR amplified using the following pairs of oligonucleotides: the forward/reverse oligonucleotide primers for PemK were PemK-F/PemK-R (Supplementary Table S1); for crystallization of the PemIK complex, a truncated PemI construct encompassing Lys57 to Ile89 was introduced, and the PemI-F/PemI-R primer pair was used for PCR. The PCR products were digested with NdeI and XhoI. The PemK gene was ligated into NdeI–XhoI-digested pET-28b(+) (Novagen, Madison, WI, USA), resulting in a twenty-residue tag (MGSSHHHHHHSSGLVPRGSH) being added to the amino terminus of the recombinant protein. We also generated PemI constructs by cloning the gene into NdeI–XhoI-digested pET-21a(+) (Novagen). The resulting plasmids were transformed into *E. coli* strain DH5α for amplification.

To identify the residues essential for the RNase activity of PemK, we mutated the Glu20, Arg25, Thr48, Thr49 and Arg84 residues to Ala by using the EZchange™ Site-Directed Mutagenesis Kit (Enzynomics, Daejeon, Korea) according to the manufacturer's protocol. The primers used for mutation are described in Supplementary Table S1.

Protein expression and purification

The recombinant PemK protein was overexpressed in *E. coli* Rossetta2(DE3) cells using Luria-Bertani culture medium. PemK expression was induced by 0.75 mM isopropyl 1-thio-β-D-galactopyranoside (IPTG), and the cells were incubated for an additional 2 h and 30 min at 37°C following growth to mid-log phase at 37°C. The cells were harvested by centrifugation at 6300 × g and frozen at –80°C. The harvested cells were resuspended in buffer A (20 mM Tris–HCl, pH 7.9 and 500 mM NaCl) containing 5% (v/v) glycerol and lysed by ultrasonication. After centrifugation at 28 300 × g for 1 h at 4°C, the supernatant containing the PemK protein was loaded on an open Ni^{2+}-NTA column (Qiagen, Hilden, Germany) pre-equilibrated with buffer A and washed with buffer A containing 100 mM imidazole. The protein bound to the column resin was eluted by an imidazole gradient (100–500 mM). The final purification step was size exclusion chromatography on a HiLoad 16/60 Superdex 200 prep-grade column (GE Healthcare, Chicago, IL, USA) in a buffer containing 50 mM Tris–HCl, pH 7.9 and 150 mM NaCl. Fractions containing PemK were pooled and concentrated to 11 mg/ml using an Amicon Ultra centrifugal filter unit (Merck Millipore, Burlington, MA, USA) for crystallization. The purity of PemK was confirmed by SDS-PAGE.

For co-expression of PemK and PemI, both plasmids, namely, PemK cloned in pET28b(+) with an N-terminal poly-His-tag and PemI cloned in pET21a(+) with no tag, were co-transformed into *E. coli* BL21(DE3), and the cells were spread on an agar plate containing both ampicillin and kanamycin. *E. coli* BL21(DE3) cells harbouring the PemIK complex protein were grown in Luria-Bertani culture medium with ampicillin and kanamycin until the OD_{600} reached 0.5−0.6 at 37°C, and protein overexpression was induced by the addition of 0.5 mM IPTG. The purification procedure used for PemK was also used to purify the PemIK protein complex. The PemIK complex labeled with selenomethionine (SeMet) was obtained by the same procedure, except that cells containing the SeMet-labeled PemIK complex were grown in M9 medium containing extra essential amino acids.

For the NMR experiments, the PemK protein was overexpressed using M9 culture medium supplemented with 1.0 g/l [U-^{13}C] glucose and 1.0 g/l [^{15}N] NH_4Cl (Cambridge Isotopes Laboratories, Tewksbury, MA, USA) as the sole carbon and nitrogen sources, respectively. To perform NMR experiments, the target proteins were purified by procedures identical to those described above except that size exclusion chromatography on a HiLoad 16/60 Superdex

200 prep-grade column (GE Healthcare) was conducted in buffer containing 20 mM Bis–Tris, pH 6.5, and 100 mM NaCl.

Crystallization and X-ray data collection

Crystals of PemK were grown using the sitting-drop vapor diffusion method at 20°C by mixing equal volumes (0.5 μl each) of the protein solution (at 11 mg/ml concentration) and the reservoir solution consisting of 20% (w/v) PEG 1000, 0.1 M potassium phosphate monobasic/sodium phosphate dibasic, pH 6.2 and 0.2 M sodium chloride. Prior to data collection, a cryoprotectant solution consisting of 20% (v/v) glycerol added to the reservoir solution was used. The crystal was vitrified in a cold nitrogen gas stream, and the data were collected using a Quantum-210 CCD detector (ADSC, Poway, CA, USA) at beamline AR-NW12A of Photon Factory, Japan. The crystals of PemK belonged to the monoclinic space group $P2_1$, with unit cell parameters of $a = 56.25$ Å, $b = 61.42$ Å, $c = 75.51$ Å, $\alpha = \gamma = 90.00°$ and $\beta = 101.20°$.

SeMet-labeled PemIK complex crystals were grown using the sitting-drop vapor diffusion method at 20°C by mixing equal volumes (0.5 μl each) of the protein solution (at 20 mg/ml) and the reservoir solution consisting of 2.0 M ammonium sulfate, 100 mM CAPS/sodium hydroxide, pH 10.5, and 200 mM lithium sulfate. Crystals were soaked in a cryoprotectant solution [the reservoir solution with 20% (v/v) glycerol]. Data collection for the SeMet-labeled PemIK complex was conducted on a Quantum-315 CCD detector (ADSC) at beamline 5C of Pohang Accelerator Laboratory, Korea. The crystal of the SeMet-labeled PemIK complex belonged to the cubic space group $F4_132$, with unit cell parameters of $a = b = c = 266.43$ Å and $\alpha = \beta = \gamma = 90.0°$. The crystallization procedure for native PemIK was the same as that for SeMet-labeled PemIK. Data collection for the native PemIK complex crystals was conducted on an EIGER 16M CCD detector (DECTRIS, Philadelphia, PA, USA) at beamline BL44XU of SPring-8, Japan. The crystal of the native PemIK complex belonged to tetragonal space group $I4_122$, with unit cell parameters of $a = b = 164.51$ Å, $c = 232.21$ Å and $\alpha = \beta = \gamma = 90.00°$.

Raw data were processed and scaled using the *HKL2000* (30) and *XDS* (31) program packages. The statistics associated with each data point are summarized in Table 1.

Structure determination and refinement

The PemK structure was solved by the molecular replacement method using the program Phaser-MR (32) with a monomer model of *E. coli* Kid (PDB code 1M1F) (33) used as the starting model at a resolution of 1.94 Å. A set of single-wavelength anomalous dispersion data from a crystal of the SeMet-labeled PemIK complex was used to solve the phase problem at a resolution of 2.8 Å. Phase calculation, density modification, and initial model building for the complex were conducted using *Autosol* and *AutoBuild* of *PHENIX Program suite* (34). The structures of PemK and the PemIK complex were refined at resolutions of 1.94 and 2.00 Å, respectively. Five percent of the data were randomly set aside as the test set for calculating R_{free} for all data (35). The models were manually modified using the program *Coot* (36) and refined with the programs *Refmac* in *CCP4 Program suite* (37,38) and *phenix.refine* in *PHENIX* (34), including bulk solvent correction. Water molecules and ligands were added using the program *Coot* (36) and were manually inspected. The stereochemistry of all models was evaluated by the program *MolProbity* (39). Interface areas and the interactions involved were calculated using *PISA* (40) and Protein Interactions Calculator (*PIC*) (41). Visualization of the structures was conducted using the program *PyMOL* (PyMOL Molecular Graphics System, version 2.0.6; Schrödinger, LLC., Cambridge, MA, USA).

Size-exclusion chromatography with multiangle light scattering (SEC-MALS)

To determine the oligomeric states of the wild-type PemK (WT) and mutants (E20A and R84A), SEC-MALS experiments were conducted using a fast protein liquid chromatography (FPLC) system (Cytiva, Marlborough, MA, USA) connected to a MiniDAWN TREOS MALS instrument (Wyatt, Santa Barbara, CA, USA). A Superdex 75 10/300 GL (Cytiva) gel filtration column was pre-equilibrated with a buffer (50 mM Tris, pH 7.9, and 150 mM NaCl,). Detector normalization was achieved using 2 mg/ml bovine serum albumin (Thermo Fisher Scientific, Waltham, MA, USA), and 200 μl of protein solution was injected at a concentration of 2 mg/ml. The data were analyzed using the ASTRA 8 software (Wyatt).

NMR experiments

A sample of PemK uniformly labeled with ^{13}C and ^{15}N was prepared in a buffer containing 20 mM Bis–Tris, pH 6.5, 100 mM NaCl, and 10% D_2O. For ^{1}H, ^{13}C and ^{15}N chemical shift assignment of backbone nuclei, a series of 3D HNCA, HN(CO)CA, HNCO, HN(CA)CO, HNCACB and HN(CO)CACB spectra were obtained at 298 K using an AVANCE 800 MHz spectrometer equipped with a cryogenic probe (Bruker BioSpin, Billerica, MA, USA). Because of the poor yield of the PemK protein, the PemK mutant R25A was additionally used to measure a series of 3D spectra for ^{1}H, ^{13}C and ^{15}N chemical shift assignment of backbone nuclei.

To determine the RNA-binding site, NMR titration experiments were conducted by measuring a set of 2D ^{1}H–^{15}N heteronuclear single quantum coherence (HSQC) spectra of ^{15}N-labeled PemK with the ssRNA UUdUAUUAA. The concentration of PemK was maintained at 0.2 mM, and the concentration of the ssRNA was increased from 0 to 0.2 mM. The titration experiments were performed at 298 K using a JNM-ECA 600 MHz spectrometer (JEOL, Tokyo, Japan). Data processing and interpretation were conducted by NMRPipe/nmrDraw (42) and NMRViewJ (43), respectively.

Fluorescence polarization (FP) assay

Serially diluted PemK and 40 nM 5′-FAM-labeled ssRNA probe (Bioneer) in a final volume of 50 μl were incubated

Table 1. Statistics for data collection and model refinement

Dataset	PemK	PemIK SeMet	PemIK
Data collection			
Wavelength (Å)	1.0000	0.9795	0.9000
Space group	$P\,2_1$	$F\,4_1\,3\,2$	$I\,4_1\,2\,2$
Cell dimensions			
a, *b*, *c* (Å)	56.25, 61.42 75.51	266.43, 266.43, 266.43	164.51, 164.51, 232.21
α, β, γ (°)	90.00, 101.20, 90.00	90.00, 90.00, 90.00	90.00, 90.00, 90.00
Resolution range (Å)	40.00–1.94 (1.97–1.94)	50.00–2.62 (2.67–2.62)	50.00–2.00 (2.12–2.00)
Total/unique reflections	150 418/37 045	1 074 093/45 479	1 465 174 /205 519
Completeness (%)	97.4 (79.8)	100.0 (100.0)	99.8 (98.9)
Redundancy	4.1 (3.6)	23.6 (24.3)	7.1 (6.7)
R_{merge} (%)[a]	10.5 (46.1)	29.2 (100)	5.7 (76.3)
Mean $I/\sigma(I)$	24.1 (3.8)	35.8 (5.2)	19.5 (2.2)
$CC_{1/2}$	0.988 (0.877)	0.973 (0.900)	1.000 (0.789)
Refinement			
Resolution range (Å)	33.95–1.94		38.77–2.00
R_{work}/R_{free}[b]	20.26/23.96		18.77/21.88
RMSDs			
Bond lengths (Å)	0.009		0.018
Bond angles (°)	1.237		1.649
Number of atoms/average *B*-factors (Å^2)			
Protein	3639/24.9		6275/44.4
Glycerol	6/26.5		6/44.9
Phosphate ion	20/29.1		
Sulfate ion			65/49.7
Water	371/33.8		515/52.8
Ramachandran plot[c]			
Most favored (%)	96.12		97.32
Allowed (%)	3.88		2.67
Outliers (%)	0.00		0.00
Rotamer outliers	0.00		0.00
PDB accession code	7EWI		7EWJ

[a] $R_{merge} = \Sigma_h\ \Sigma_i\ |\ I(h)_i - <I(h)>\ |\ /\ \Sigma_h\ \Sigma_i I(h)_i$, where $I(h)$ is the intensity of reflection h, Σ_h is the sum over all reflections, and Σ_i is the sum over i measurements of reflection h.
[b] $R = \Sigma\ |\ |F_{obs}| - |F_{calc}|\ |\ /\ \Sigma\ |F_{obs}|$, where R_{free} is calculated for a randomly chosen 5% of reflections, which were not used for structure refinement and R_{work} is calculated for the remaining reflections.

at room temperature for 20 minutes in a buffer containing 50 mM Tris, pH 7.9, and 150 mM NaCl. All experiments were performed in triplicate. FP was analyzed using a SpectraMax M5 plate reader (Molecular Devices, San Jose, CA, USA) by measuring the parallel fluorescence emission (F =) and perpendicular fluorescence emission (F⊥) at 530 nm (excitation at 485 nm), and the FP value was calculated using Equation (1). To calculate K_d values, non-linear regression was used to fit the anisotropy data (y) as a function of total protein concentration (x) by *KaleidaGraph* software (Synergy Software, Reading, PA, USA) according to Equation (2) (44), where m_1 and m_2 are the minimum and maximum anisotropy values, respectively, and m_3 is the K_d value.

$$\mathrm{FP\,(mP)} = 1000 \times \frac{F_{=} - G \cdot F_{\perp}}{F_{=} + G \cdot F_{\perp}} \quad (1)$$

$$y = m_1 + (m_2 - m_1) \times \frac{x}{m3 + x} \quad (2)$$

In vitro RNase activity assay

To monitor the RNase activity of PemK, a fluorescence quenching assay was conducted on the WT PemK and its mutants using the RNase Alert Kit (IDT, Coralville, IA, USA) at 37°C for 30 min. The assays were performed in a buffer containing 20 mM Tris, pH 7.5 and 150 mM NaCl. The 20 μl reaction mixture contained 0.35 μM PemK (WT or mutants) with an RNA concentration range of 0.1–2.0 μM. A fluorophore covalently attached to a synthetic RNA strand was quenched by a quencher group attached to the other end. When the RNA was digested by an RNase, the fluorophore was released from the quencher. The released fluorophore emitted fluorescence at 520 nm upon excitation at 490 nm. The fluorescence was measured as RFU on a SpectraMax M5 plate reader (Molecular Devices). Michaelis–Menten kinetics was used to analyze the initial velocities and kinetic parameters K_m and k_{cat} using *KaleidaGraph* software (Synergy Software).

Molecular docking for binding mode analysis

The HADDOCK 2.2 webserver (45) was used to generate an ssRNA-bound PemK model. The obtained crystal structure of the apo form of PemK was used as an input model together with a model ssRNA UUdUAUUAA, which was slightly modified from the ssRNA UUdUACAUAA that forms a complex with *Bacillus subtilis* MazF (PDB code 4MDX) (46). The AIR file was generated based on the following residues as active residues: Arg19, Glu20, His22, Arg25, Met34, Thr49, Arg50 and Tyr107 of PemK and dU3, A4, U5, and U6 of the ssRNA. Passive residues were designated automatically. Residues 12−25, 35−43, 50−56 and 98−110 in the PemK protein and all residues of the ssRNA were defined as semi-flexible residues.

The default setting for sampling and clustering was used to obtain the model structure. The number of clusters for rigid-body docking was 1000. The number of structures for semi-flexible residues and explicit solvent refinements was 200 each. We used the Fraction of Common Contacts (FCC) for the clustering step with a 0.6 cut-off and a minimum clustering size of 4.0.

Molecular dynamics (MD) simulation and MM/GBSA

To study the RNA recognition and PemI binding of PemK, triplicate runs of 300 ns MD simulations for three types of structures, PemK, PemIK and ssRNA-bound PemK, were conducted. Three protein models were prepared using Protein Preparation Wizard (47) in the Schrödinger suite. All MD simulations were conducted using Desmond (48) in Schrödinger suite 2020-4. For explicit solvent simulations, the periodic boundary condition using dimensions of 10 × 10 × 10 Å^3 was applied. The system was solvated with water using the TIP3P water model and 150 mM NaCl after it was electrically neutralized with sodium (or chloride) ions. The solvated system was energy-minimized and relaxed for 100 ps using the minimization step of Desmond with the OPLS2005 force field (49). MD simulations were performed in the NPT (isothermal and isobaric simulation) ensemble, where the Martyna–Tobias–Klein method (50) and Nose-Hoover thermostat algorithm (51) were used to establish an isotropic pressure (1 atm) and constant temperature (300 K), respectively. Then, 300 ns simulations for PemK, PemI-neutralized PemK and ssRNA-bound PemK were run and saved as trajectories at 300 ps intervals with three independent replicates. The trajectories were analyzed using Simulation Event Analysis and Simulation Interaction Diagram in Desmond.

Binding free energies (ΔG_{bind}) of ssRNA or PemI against PemK were computed using the Molecular Mechanics/Generalized Born Surface Area (MM/GBSA) method. First, each protein complex extracted from the crystal structure of PemI-neutralized PemK or the docking structure ssRNA-bound PemK was prepared using Protein Preparation Wizard (47) in the Schrödinger suite. For the binding free energy calculation, the solvation model of VSGB (variable-dielectric generalized born model) with the force field of OPLS4 (52) was applied, and flexible residues within a distance of 3 Å around ligands were defined in the protein models. All binding free energy calculations via the MM/GBSA method were conducted using the Prime (53) MM/GBSA module in Schrödinger suite 2021-2.

RESULTS

Structural analysis of the *S. aureus* PemK

Our initial approach included determination of the PemIK complex structure, involving successful solubilization, purification, and structural analysis of the PemIK complex and PemK. Before acquiring the PemIK complex structure, we obtained the structure of the toxin protein PemK at a resolution of 1.94 Å. The refined model of PemK accounts for four monomers, which form two dimers (A/B chains and C/D chains), with four phosphate ions and one glycerol in the asymmetric unit (Figure 1A). The refinement statistics are summarized in Table 1. Each monomer of PemK exhibits pair-wise backbone root mean square deviations (RMSDs) of 0.09−0.31 Å for 110−111 Cα atom pairs. PemK adopts an SH3-like barrel fold consisting of a seven-stranded, twisted, antiparallel β-sheet in the order β7–β1–β2–β3–β5/β6–β4 and surrounded by two α-helices (α1 and α2) (Figure 1B).

The interface areas among the four monomers (chains A−D) in the PemK structure indicate that two stable dimers (dimers A/B and C/D) exist in the asymmetric unit. The interface area between chains A and B (or between C and D) is 1723 Å^2 (or 1712 Å^2) for the PemK dimers, while the interface area of the other possible pairs A/C, A/D, B/C and B/D are 288, 0, 406 277 Å^2, respectively. The dimeric structures of the PemK crystals were in good agreement with the SEC-MALS results, which showed the dimeric forms in solution (Supplementary Figure S1A). In the dimerization interfaces of PemK (chains A/B and chains C/D), hydrophilic and hydrophobic interactions are present, as shown in Figure 1C. Residues on α1, α2, β3, L12, L56 and L67 are mainly involved in the formation of the dimeric interface. L12, L56, and L67 are the loops in β1/β2, β5/β6 and β6/β7, respectively. Eighteen residues are related to hydrophilic interactions, namely, Gln5, Arg19, Glu20, Asn32, Gln33, Met34, Thr39, Trp43, Val74, Ile76, Ala78, Asp80, Arg84, Thr106, Tyr107, Leu108, Lys109 and Thr111. All of the hydrophilic interactions are hydrogen bonds. Ten residues contribute to hydrophobic interactions, namely, Pro15, Phe41, Trp43, Val74, Ile76, Leu101, Ile104, Tyr107, Leu108 and Pro110. Among the residues in the dimerization interfaces, Arg19, Glu20, Asp80 and Arg84 interact with each other and neighboring residues via strong and extensive hydrophilic interactions (Figure 1C). However, E20A and R84A mutations did not principally cause dissociation of the PemK dimer as shown in the SEC-MALS results (Supplementary Figure S1B and C). The four residues are positioned in two loops (Arg19 and Asp20 in L12; Asp80 and Arg84 in L67). These two loops may play important roles in complexes with either RNA or the cognate antitoxin PemI, which can be accompanied by the movement of two loops, especially in the case of PemI binding (details are discussed in the section titled 'L12 in PemK play a decisive role in the formation of the PemIK complex').

Structural comparison of *S. aureus* PemK with its homologs

When the *S. aureus* PemK structure was compared with those of its homologs using the Dali server (2), *E. coli* MazF (PDB code 5CR2) (49) showed the highest structural similarity with PemK, showing *Z*-scores of 16.4−16.7. The next highest Z-score was 16.6, acquired from *E. coli* Kid (PDB code 1M1F) (33). *S. aureus* MazF (PDB code 4MZM) (50) and *B. subtilis* MazF (PDB code 4MDX) (46) also displayed similar *Z*-scores, with values of 15.5−15.8 and 15.6−15.8, respectively. The structure of PemK also shared similarity with that of *B. anthracis* MoxT (PDB code 4HKE) (51). Detailed statistics for structural comparison of PemK with its homologs are provided in Supplementary Table S2.

Although PemK and its homologs share conserved residues, as shown by sequence alignment (Figure 2A), and exhibit similar folds (Figure 2B), differences in secondary

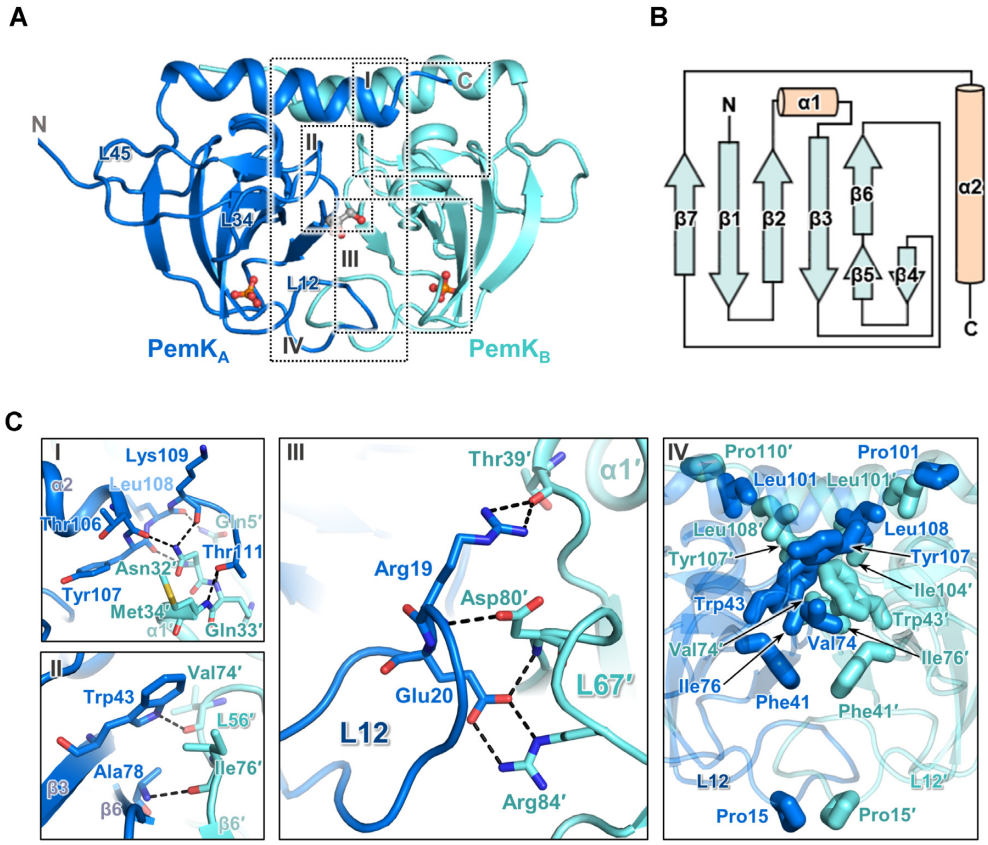

Figure 1. Overall structure of PemK. (**A**) Overall structure of the PemK dimer. Chains A and B are represented in blue and cyan, respectively. Phosphate ions (orange) and a glycerol molecule (grey) are shown in a ball and stick representation. The regions depicted in (C) are marked as squares with each label. (**B**) Diagram of the secondary structure of the PemK monomer. The PemK monomer consists of two α-helices and seven β-strands forming SH-like barrel folds. α-Helices and β-strands are colored light orange and cyan, respectively. (**C**) Dimerization of PemK. The regions containing hydrogen bonds in the PemK dimer are shown in I, II and III. The residues involved in hydrophobic interactions are represented in IV.

structures exist among them. The long loop between β1 and β2 (L12) plays an essential role in controlling the PemI or RNA binding. In the PemK dimer, L12s are held by each other via the formation of hydrogen bonds with L67 like a gate, which facilitates RNA binding. Interestingly, L12 controls the binding of the antitoxin PemI, as described later. The loop between β3 and β4 (L34) and the loop between β4 and β5 (L45) also show large Cα RMSDs of 10.1 and 6.8 Å for residues Arg53 and Gly65, respectively, compared to the equivalent segments in *E. coli* Kid (Figure 2C). L34 of PemK faces L12. Some homologs, such as *Bacillus anthracis* MoxT and *B. subtilis* MazF, have 3_{10}-helices instead of the loop. Additionally, most homologs have 3_{10}-helices in the region corresponding to L67, except *E. coli* MazF and PemK.

The structures of MazF from *B. subtilis* and *E. coli* were bound to RNA and DNA analogs, respectively. The nucleotide-binding region was composed of the interface between L12 and L34 of one monomer and α1 of the other monomer. The electrostatic potential surface of the predicted nucleotide-binding region in *S. aureus* PemK also exhibited differences compared with those in the homologs (Figure 2D). Most homologs possessed crevices in the interfaces between monomers, corresponding to L12 and L34 of the *S. aureus* PemK dimers. In particular, *S. aureus* PemK has a distinct positively charged patch in this region in contrast to the other homologs. Additionally, the difference in the loop lengths of L12 and L34 makes the crevice of *S. aureus* PemK dissimilar to those of the homologs. The distinctive structural dissimilarity of *S. aureus* PemK may be related to determinants of the mRNA sequences. We observed that structures of L34 and L45 are not affected by crystal packing in both the PemK and PemIK complex structures.

S. aureus PemK shows RNA-binding and RNase activities

The crystal structure of the toxin protein PemK was obtained in phosphate ion-bound form. The structures show that residues Arg25 in β2, Thr48 in β3, and Thr49 in L34 form hydrogen bonds with phosphate ions between L12 and L34, which are adjacent to the putative active site (Figure 3A). Interestingly, structural superimposition of *S. aureus* PemK with sulfate ion-bound *B. anthracis* MoxT (PDB code 4HKE) (51) and phosphate ion-bound *E. coli* Kid (PDB cod 1M1F) (33) revealed that the coordinate of the phosphate ion in *S. aureus* PemK is identical to those of the sulfate ion in *B. anthracis* MoxT and phosphate ion in *E. coli* Kid (Figure 3B). Overlay with the structure of RNA-bound MazF from *B. subtilis* (PDB code 4MDX) (46) showed that the negatively charged phosphate ion of

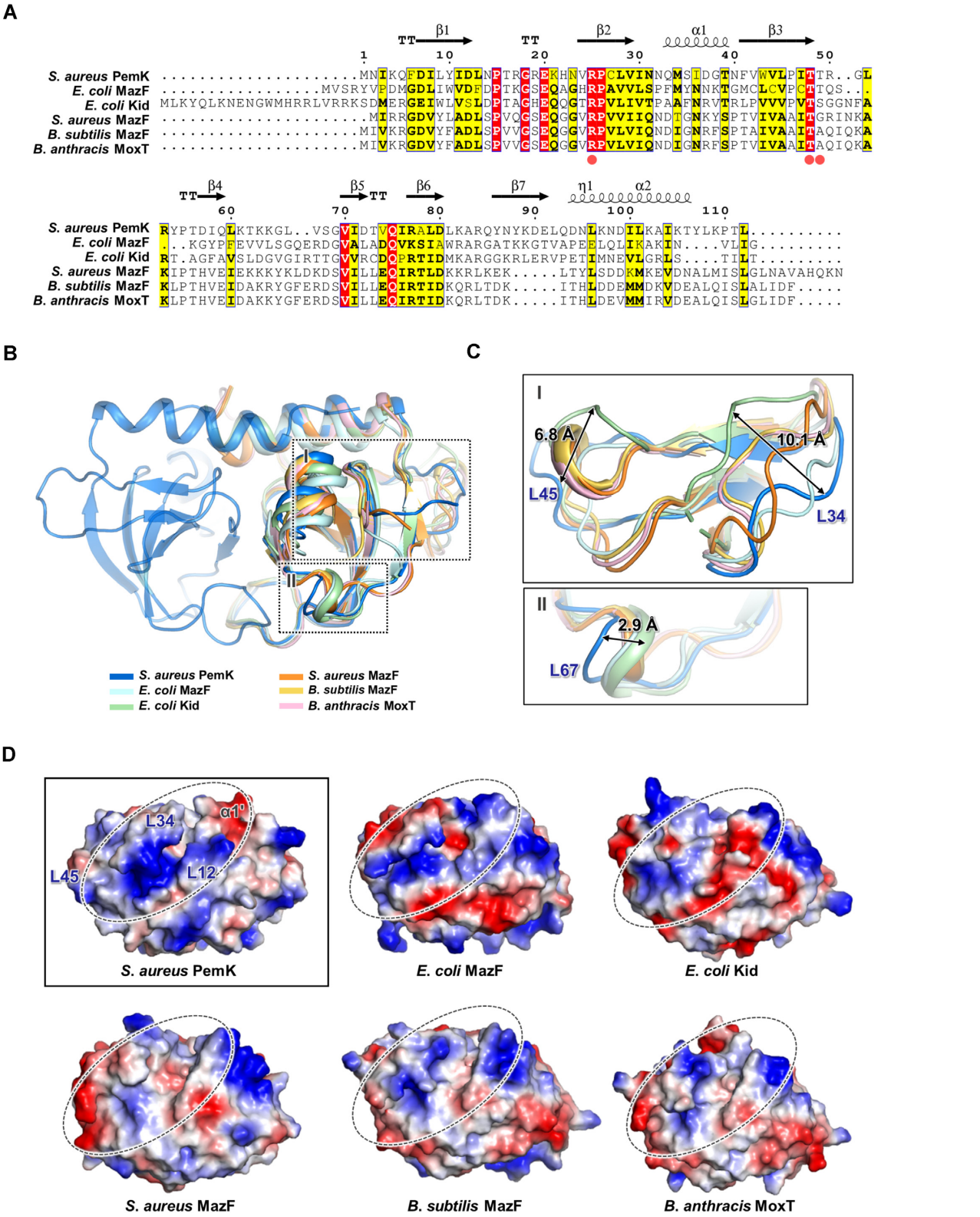

Figure 2. Structural comparison of PemK with its homologs. (**A**) Sequence alignment of PemK with its homologs. Secondary structures are denoted in the upper region. Potential active site residues are marked as red circles. Conserved and similar residues are shown in red and yellow boxes, respectively. TT and η1 refer to a β-turn and a 3_{10}-helix, respectively. Sequence alignment and visualization were conducted using Clustal Omega (61) and ESPript 3.0 (62). (**B**) Overlay structure of PemK with other homologs. *S. aureus* PemK (light blue), *E. coli* MazF (cyan), *E. coli* Kid (light green), *S. aureus* MazF (orange), *B. subtilis* MazF (yellow), and *B.* anthracis MoxT (pink) are shown. (**C**) Loop regions of PemK and its homologs. The regions exhibiting distinct features in (B) are shown in boxes I and II. (**D**) Electrostatic surface potential represents different charge distributions between the L34 and L12 regions in PemK and its homologs. The positive crevice regions are highlighted in dotted circles.

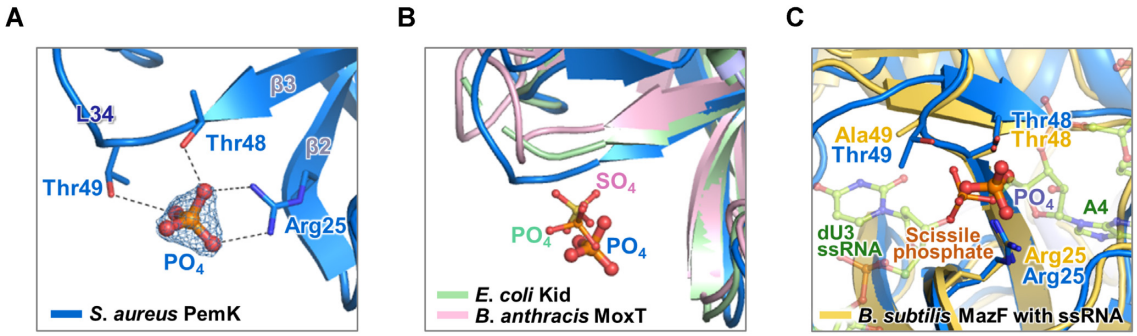

Figure 3. Active site of PemK and its homologs. (**A**) Putative active site of PemK. The $2F_o - F_c$ electron density map contoured at 1.5σ around PO_4 was drawn with the model. The hydrogen bonds between PO_4 and the putative active site residues Arg25, Thr48, and Thr49 are depicted as dashed grey lines. (**B**) PO_4 of *E. coli* Kid and SO_4 of *B. anthracis* MoxT are overlaid with PO_4 of *S. aureus* PemK. (**C**) Overlay of *S. aureus* PemK and *B. subtilis* MazF with ssRNA. The position of the scissile phosphate of ssRNA in *B. subtilis* MazF was well matched with the position of PO_4 in *S. aureus* PemK.

S. aureus PemK matched the scissile phosphate between dU3 and A4 of the bound RNA in the *B. subtilis* MazF structure (Figure 3C). The residues involved in the interactions are also similar between the two structures. These insights indicate that this location is the possible active site of PemK.

It is known that the toxin PemK plays a role as a ribosome-independent RNase that recognizes a specific sequence, U↓AUU (17). To investigate the residues that contribute to the RNase activity of PemK, point mutagenesis of PemK was conducted. For this purpose, we mutated residues Arg25, Thr48 and Thr49, which form hydrogen bonds with a phosphate ion, to Ala. Because Arg84 is also considered a key residue (17), the hydrogen bond pairing residue Glu20 was mutated to Ala. Using these mutants, a fluorescence quenching assay was carried out to determine the effects of the mutations on RNase activity in the potential active site of PemK. As shown in Figure 4A, all of the mutants led to the detectable loss in RNase activity. The mutants exhibited ∼40–60% reduced RNase activity. The K_m and k_{cat} values of the WT PemK were 0.65 μM and 13.0 RFU min^{-1} μM^{-1}, respectively. All of the mutants showed increased K_m values and decreased k_{cat} values, compared with those of the WT PemK, which indicates that all of the mutants may be involved in catalytic activity. The mutant enzymes show reduced efficiencies with 1.5- to 3.3-fold decreased k_{cat}/K_m values. The mutation of Arg25 and T49A yielded increases in K_m by 1.1- to 1.9-fold and decreases in k_{cat} by 1.3-fold, while E20A, T48A, and R84A mutants exerted >3-fold increases in K_m and minor decreases in k_{cat} values. The data analyzed using Michaelis–Menten kinetics are summarized in Table 2.

Additionally, we measured the RNA-binding ability of PemK (WT) and its mutants (E20A, R25A, T48A, T49A and R84A) using an FP assay (Figure 4B). As mentioned above, these five mutants showed reduced RNase activity. The FP assay with an uncleavable 8-mer ssRNA showed that mutation of R25A and R84A led to 35- to 30-fold weaker RNA-binding ability than that of the WT protein. The E20A and T48A mutant showed 4.0- to 16-fold reduction in RNA-binding affinity. In contrast, mutation of Thr49 to Ala led to a similar affinity for the RNA substrate as that of the WT protein. In PemK, we found that E20A, Arg25, Thr48, and Arg84 are key residues for RNA-binding and catalytic activities.

Predictive model for RNA binding by PemK

In an effort to reveal the RNA-binding site of PemK, we tried to co-crystallize RNA and PemK. It was previously demonstrated that PemK recognizes the specific target sequence U↓AUU (17). To avoid cleavage of the target sequence during crystallization, we used the extended ssRNA UUdUAUUAA, in which the scissile uracil was modified to the deoxy form. Unfortunately, we could not observe any electron density corresponding to the ssRNA. Therefore, NMR titration experiments were conducted to gain insights into the binding between PemK and RNA. ^{15}N-labeled PemK was titrated with increasing concentrations of the ssRNA at 1:0.1, 1:0.4, and 1:1 molar ratios. As shown in Supplementary Figure S2, the NMR peaks of PemK titrated with the ssRNA exhibited slow exchange behavior. Because significant changes in chemical shift were not observed on all residues in the spectra, we compared the differences in peak intensity (Figure 4C). Overall, the peaks exhibited a decrease in intensity with RNA binding. In particular, the peaks for Ile3, Arg19, Met34, Arg50 and Tyr107 almost disappeared upon the addition of 1:1 (molar ratio) ssRNA. Asp12, Thr16, Glu20, Lys21, Asn23, Asp37 and Val42 exhibited significantly low peak intensities. In conclusion, we found that the residues on L12 were significantly affected upon RNA binding. On the electrostatic potential surface of PemK, the positively charged residues are distributed along L12 and L34 (Figure 2D), which is consistent with the loss of peak intensity corresponding to these residues.

To obtain structural insights into the PemK-RNA interaction in more detail, we built an RNA-bound PemK model using the HADDOCK 2.2 webserver (45). The results of NMR titration and mutational assays were utilized as input parameters, and the modified RNA substrate from the *B. subtilis* MazF-RNA complex (PDB code 4MDX) (46) was used as an RNA model. Details regarding the docking process are described in the Materials and methods section. The structure with the lowest HADDOCK scores was selected for further refinement. The HADDOCK score of the

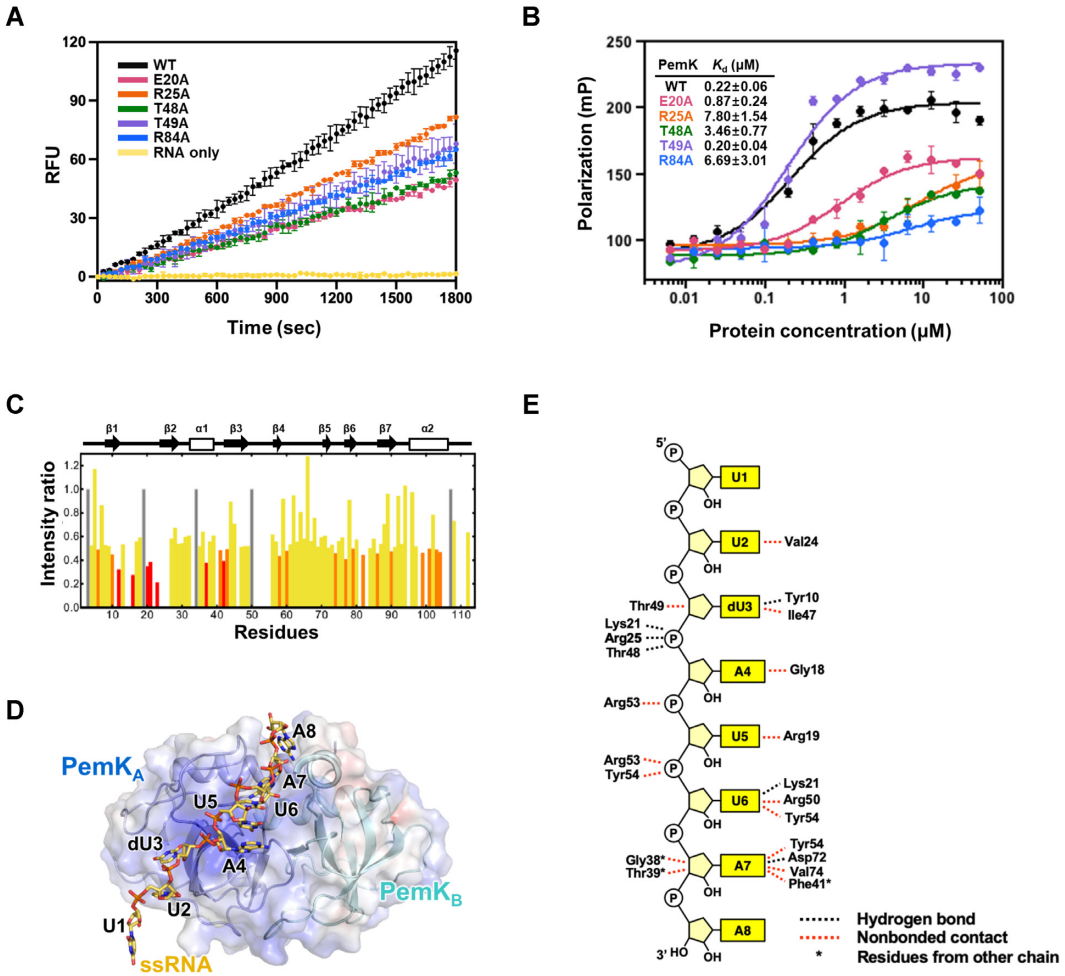

Figure 4. RNA binding and cleavage of PemK. (**A**) RNase activity assay of PemK WT and its mutants. The colors indicating specific PemK mutants used in the graph are represented in the figure. (**B**) RNA-binding affinities of PemK WT and its mutants. A fluorescence polarization assay was used to monitor the affinity. (**C**) The comparison of the NMR peak intensities of residues in PemK upon ssRNA binding (1.0 equivalent) with those without ssRNA binding was plotted according to residue number. The secondary structural elements of PemK are shown above the plot. (**D**) ssRNA-bound PemK dimer structure produced by the HADDOCK 2.2 webserver. The PemK dimer is represented in cartoon and surface views, and the ssRNA is shown as a stick model. The ssRNA-bound region of PemK exhibited a positively charged distribution. (**E**) NUCPLOT diagram of contacts between ssRNA and PemK. Black and red dotted lines represent hydrogen bonds and nonbonded contacts (<3.35 Å), respectively. Residues of chain B are marked with '*'.

Table 2. Comparison of kinetic parameters of WT and mutants of PemK

PemK	k_{cat}[a]	K_m[a]	k_{cat}/K_m
WT	13.00	0.65	20.0
E20A	12.62	>2.0[b]	<6.31[b]
R25A	9.80	0.74	13.24
T48A	12.39	>2.0[b]	<6.20[b]
T49A	9.96	1.22	8.16
R84A	12.05	>2.0[b]	<6.03[b]

[a]The units of k_{cat} and K_m are defined as RFU min^{-1} μM^{-1} and μM, respectively.
[b]Due to the solubility of RNA substrates, accurate values of K_m and k_{cat}/K_m cannot be determined.

final PemK-RNA complex was –155.3 ± 3.3. The van der Waals and electrostatic energy values were –83.3 ± 3.2 and –368.6 ± 18.7 kcal·mol^{-1}, respectively. Overall, HADDOCK provided one possible model and revealed that one ssRNA was bound to the PemK dimer throughout the positively charged patch. The ssRNA was predicted to bind to the residues that were mainly positioned in L12 and L34 from one PemK monomer and L67 from another monomer (Figure 4D). The interactions between PemK and the central four nucleotides dUAUU consist of five hydrogen bonds and nine van der Waals contacts (Figure 4E). The O_2P oxygen of the scissile phosphate of A4 forms three hydrogen bonds that are formed directly with the N_Z atom of Lys21, NH_1 atom of Arg25, and OG_1 atom of Thr48. Among these residues, Arg25 and Thr48 are well-conserved residues in homologs according to the sequence alignment (Figure 2A). The O_2' atom of dU3 also forms hydrogen bonds with the NH_1 atom of Arg25 and the OG_1 atom of Thr49.

To validate the model, we performed MD simulations for the PemK-RNA complex. During the MD simulation, the interactions, including H-bonds, hydrophobic, ionic, and water bridges, represented as the number of contacts between PemK and RNA, were sustained for 300 ns (Figure 5A). Additionally, the variations of RMSD and ra-

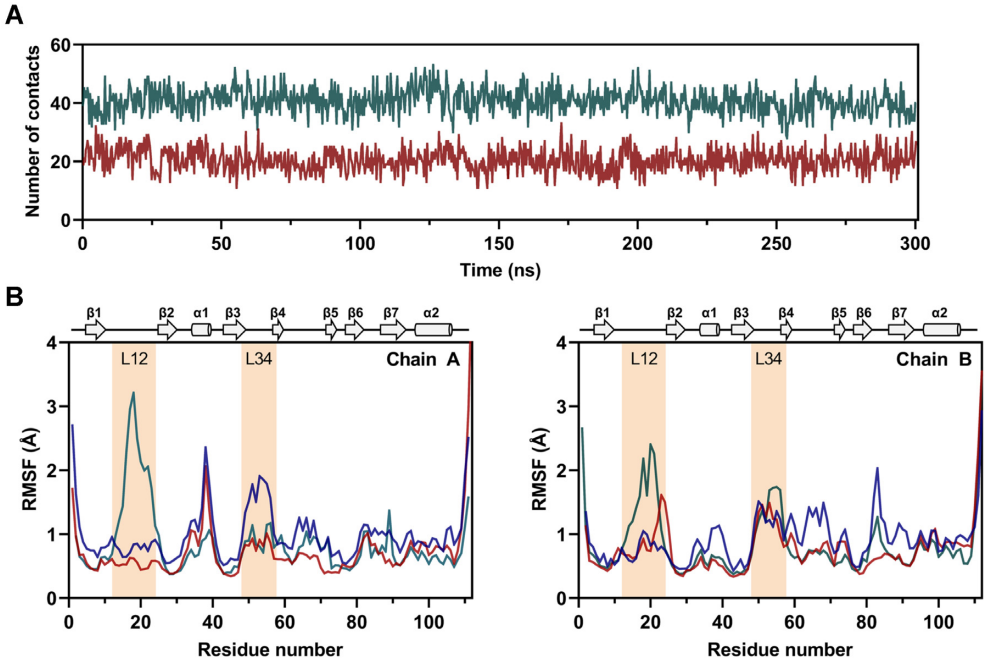

Figure 5. Comparison of MD simulations for PemK, PemI-neutralized PemK, and ssRNA-bound PemK. (**A**) The number of contacts between PemK and PemI (green) or PemK and ssRNA (red) over 300 ns MD simulations. The contacts that include hydrogen bonds, hydrophobic contacts, ionic interactions, and water bridges are calculated from the Simulation Interactions Diagram built in the Desmond of Schrodinger suite. (**B**) RMSF analysis of PemK, PemI-neutralized PemK, and ssRNA-bound PemK. The RMSF values of the Cα atoms were plotted as a function of residue for chains A (left) and B (right), respectively. PemK, PemI-neutralized PemK, and ssRNA-bound PemK are colored in blue, green, and red, respectively. The secondary structural elements of PemK are shown above the plot and the regions for L12 and L34 are indicated with colored boxes. All MD simulations were repeated three times and yielded similar results.

dius of gyration for the models are presented and indicate structural stability during the MD simulations (Supplementary Figure S3A and S3B). We calculated the interacting contacts and binding free energy using the MM/GBSA approach. The calculated ΔG_{bind} energy of ssRNA-PemK (-58.3 kcal/mol) was higher than that of the PemIK complex (–232.5 kcal/mol), indicating that the binding of antitoxin against PemK is favored with lower binding energy than that of ssRNA. In the dynamic state, Arg25 and Thr48 showed significant contacts with RNAs, which is similar to the result obtained from the analysis of model structure (Supplementary Figure S4). Additionally, a residue root mean square fluctuation (RMSF) was calculated to characterize the residual contribution to the binding (Figure 5B). In the comparison of PemK and ssRNA-PemK, the overall RMSF was decreased when RNA was bound to PemK. Particularly, RMSF on L34 of chain A was significantly decreased when RNA was bound to PemK, which suggests the direct involvement of the region of PemK in ssRNA binding.

The *S. aureus* PemI monomer neutralizes the PemK dimer by forming a structural complex

To reveal the mechanism underlying the neutralization of PemK by PemI at the molecular level, we performed extensive crystallization of the PemIK protein using a number of constructs, including full-length PemI. After X-ray experiments on various crystal samples, we successfully found that crystallization between the truncated construct Lys57−Ile89 of PemI and the full-length PemK led to the clear observation of electron density from both protein crystals. The solved structure of PemK in complex with PemI was refined at a resolution of 2.00 Å (Table 1). The asymmetric unit comprises three PemI monomers (chains C, F and I), three PemK dimers (chains A/B, D/E, and G/H), 13 sulfate ions and one glycerol molecule.

The structure of the PemK monomer from the PemIK complex has the same secondary structural composition observed in the PemK structure without PemI. The structure of the PemI monomer comprises one α-helix (α1, residues 60−70) (Figure 6A). The interface of two PemI monomers has only one hydrophobic interaction from each Phe67 residue. The antitoxin PemI binds tightly to the toxin PemK dimer with an interface area of ∼1920 Å^2. The intrinsically disordered C-terminal region of PemI is aligned along the concave surface between PemK dimers (Figure 6A). In the PemI–PemK interface, the side-chain atoms of residues Phe67, Tyr74, Trp81, Val85 and Ile89 of PemI interact with the hydrophobic region of PemK (Figure 6B). Residues from Tyr74 to Ile79 of PemI form hydrogen bonds and salt bridges extensively with hydrophilic residues in the dimerization surface of the PemK dimer (Figure 6B). In particular, Arg77, Asp80 and Arg84 from chains A and B of PemK form hydrophilic interactions with PemI.

There is no known PemIK complex in other species. Therefore, three complex structures, MazEF from *E. coli* (PDB code 1UB4) (53), MazEF from *B. subtilis* (PDB code E7) (46), and MazEF4 from *M. tuberculosis* (PDB code 5XE3) (54), were compared with the PemIK complex, as

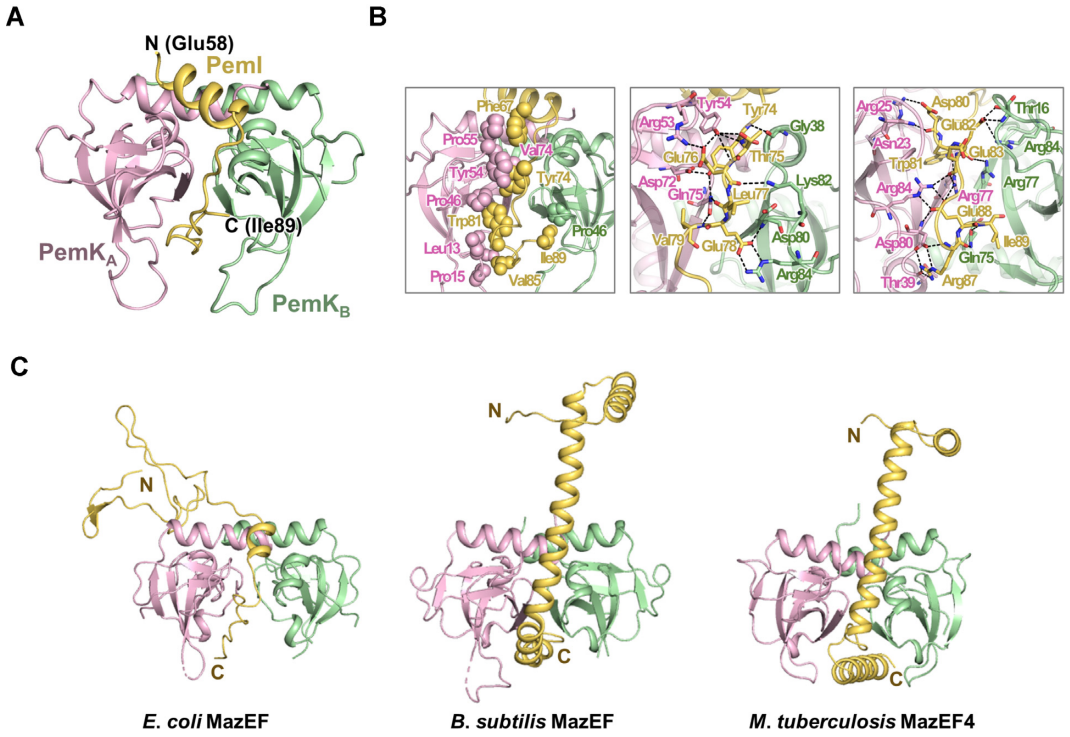

Figure 6. Overall structure of the PemIK complex. (**A**) Overall structure of PemIK. The PemIK complex, composed of two PemK dimers and one PemI monomer (residues from Lys57 to Ile89), is shown. (**B**) Interactions between the PemK dimer and PemI monomer. Residues (shown as spheres) contributing to hydrophobic interactions in the PemIK complex are shown in the left rectangle. The residues involved in hydrogen bonds within the PemIK complex are indicated in the middle and right boxes. Hydrogen bonds are shown as black dashes. (**C**) Homologs of the PemIK complex. The toxin dimers [monomer A (pink) and monomer B (light green)] and antitoxin monomer (yellow) are represented.

shown in Figure 6C. Interestingly, each antitoxin showed a dissimilar binding mode with its cognate toxin protein, although the three toxin proteins shared a highly similar structural architecture. Among the three compared complexes, the binding mode of *S. aureus* PemI was similar to that of *E. coli* MazE. In both *S. aureus* PemI and *E. coli* MazE, one short α-helix and a long disordered C-terminal coil participated in toxin binding by covering the dimerization interface of the toxin. According to the sequence-based structural motif, the antitoxins *S. aureus* PemI and *E. coli* MazE contain the SpoVT-AbrB domain, while *B. subtilis* MazE and *M. tuberculosis* MazE4 contain a ribbon-helix-helix domain.

Loop L12 in PemK plays a decisive role in the formation of the PemIK complex

The interfaces of the PemK dimer in the PemI-neutralized PemK dimer ($PemK_{open}$) largely deviated from those in the PemK dimer without PemI ($PemK_{closed}$). The interface area of $PemK_{open}$ was ∼1160 Å^2, while that of $PemK_{closed}$ was ∼1720 Å^2. This difference might have originated from the conformational change and movement of L12 of PemK upon PemI binding, which causes structural rearrangement of PemK by switching to the $PemK_{closed}$ conformation from $PemK_{open}$ (Figure 7A and Supplementary Figure S5). In $PemK_{closed}$, loop L12 adopts a 'closed form' by interacting with residues on L67 and can be involved in RNA substrate binding (Figure 7A).

The conformational change from $PemK_{open}$ to $PemK_{closed}$ is followed by the striking preference for a cis-peptide bond between Asn14 and Pro15 (Figure 7B and C). The cis-peptide is observed only in the $PemK_{closed}$, driving intra- and inter-protein interactions around L12 in a specific way that determines the 'closed' conformation, with accommodation of PemI binding. In $PemK_{closed}$, Pro15 in PemK makes extensive hydrophilic interactions with Asp12, Asn14 and Arg84 and hydrophobic interactions with Leu13, Leu79 and Pro15′, leading to zipping up of the PemI-binding site with more interactions of Thr39/Asp80/Arg84 ($PemK_A$) and Arg19/Glu20 ($PemK_B$) (Figure 7B). In the open form of $PemK_B$, Pro15 forms hydrophilic intermolecular contacts with Thr16, Arg19, and Arg84, leading Asn14 to have extensive hydrophilic interactions with Asp12, Lys21, Asn23 and Arg84 (PemI). Pro15 in $PemK_A$ interacts with Asp12, Asn14 and Thr16 in a hydrophilic manner and makes hydrophobic contacts with Leu13 (Figure 7B).

Interestingly, we observed that PemI mimics the L12 gate in PemK by replacing the L12 residues of PemK with the residues of PemI when we superimposed $PemK_{open}$ and $PemK_{closed}$ of the PemK structures. Instead of Glu20 in PemK, Glu78 in PemI interacts with Asp80 and Arg84 in PemK. Arg87 in PemI interacts with Thr39 instead of Arg19 in PemK. These two residues of PemI occupy a nearly identical position in L12 of PemK, forming an 'open' conformation of PemK (Figure 7C). By forming new interactions between PemI and PemK, Arg25 and Arg84, which affect the

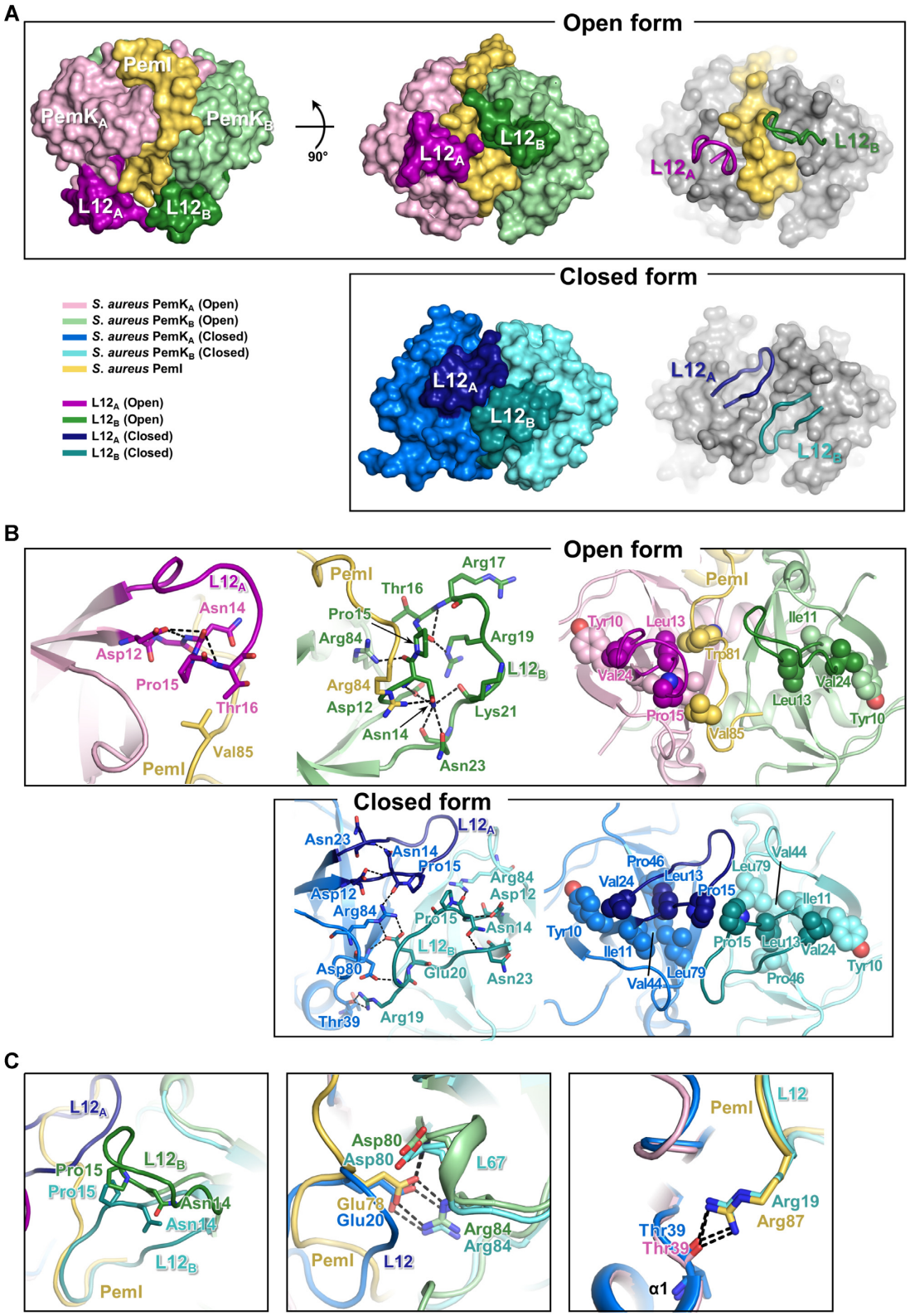

Figure 7. Conformational change of PemK upon PemI binding. (**A**) PemK and PemIK complex structures in surface view. In the open form of PemK in the PemIK complex, toxins are represented in pink (monomer A) and light green (monomer B). In the closed form, two PemK monomers are colored light blue (monomer A) and light cyan (monomer B). The antitoxin PemI is represented in yellow. The L12 loops of PemK are highlighted in darker colors (in $PemK_{open}$, magenta, and green; in the closed form, dark blue and cyan). When PemI binds to PemK, the L12 loops of PemK undergo conformational changes from $PemK_{closed}$ to $PemK_{open}$. (**B**) Difference in peptide bonds between Asn14 and Pro15. The residues contributing to hydrophilic interactions are shown with each interaction (black dashes). The residues related to hydrophobic interactions are indicated as spheres. (**C**) Replacement of PemK residues by PemI residues. Some key residues involved in PemK dimerization are replaced by PemI residues in the PemIK complex structure. The hydrogen bonds in the PemK dimer and PemIK complex are shown in black dashes.

RNase activity of PemK, were blocked by hydrophilic interactions with neighboring PemI residues, resulting in the neutralization of PemK toxicity. In addition to the large conformational change in loop L12, slight movements in loop L34 and loop L67 of PemK were also observed upon PemI binding. The movement of loops outward, away from PemI, would result from not only the interaction of PemK residues with PemI but also the flexible nature of the loop regions (Supplementary Figure S5).

To monitor the dynamic property of PemIK, MD simulations for the PemIK complex were performed. The overall numbers of contacts between PemK and antitoxin PemI were maintained (Figure 5A), and the significant variations of RMSD and radius of gyration for the PemIK structure were not shown (Supplementary Figures S3A and B) during 300 ns simulation. Additionally, as shown in Figure 5B, RMSF on L12 in the structure of the PemIK complex ($PemK_{open}$) was distinctively increased compared with those in PemK ($PemK_{closed}$). These results indicate that L12 of $PemK_{open}$ is more dynamic than L12 of $PemK_{closed.}$ with a flexibility increase. However, the significant decrease in RMSF at L34 of chain A observed in the structure of PemIK revealed that the region becomes more stable upon binding to PemI (Supplementary Figure S5).

DISCUSSION

The *S. aureus* PemIK TA module was first discovered in the low-copy-number plasmid R100. The two corresponding genes located near the replication origin are involved in the stable maintenance of R100. In the genus *Staphylococcus*, a recent study revealed, based on bioinformatics analyses of protein sequences, that the *pemIK* locus is located in not only plasmids but also chromosomes (28).

In this study, we present PemK and PemI-neutralized PemK structures and detailed mechanistic evidence regarding PemK activity and the interference of PemI. The results show that PemK-related proteins, exhibiting a common structural fold, possess unique methods of conducting physiological activities in each organism. In particular, we reveal the importance of the long loop L12 and a large conformational change in L12, which was confirmed by structural comparison between PemK and the PemIK complex. Additionally, MD simulation results also support the flexible property of L12 of PemK. L12 of PemK may play a gating role for PemI antitoxin binding. One of the findings among PemK homologs was the flexibility and length of loops L34, L45 and L67. Additionally, a different distribution of positively charged residues in the crevices on the PemK surface also exists. These characteristics of toxin proteins might determine the conformation for binding the specific RNA or antitoxin.

Several previous studies have revealed the catalytic residues of PemK homologs. In MoxT from *B. anthracis*, His59 and Glu78 were predicted to be the catalytic acid-base couple, and the stabilizing residues were Gln21 and Gln79 (55). In Kid from *E. coli*, it was reported that RNA cleavage involves uracil 2′ OH from RNA, the catalytic acids are Arg73 and His17, and the catalytic base is Asp75 (56). However, these residues were not found to be conserved when sequence alignment of PemK with its homologs was performed. Other residues, namely, Arg25 and Thr48 in PemK from *S. aureus*, are conserved as Arg25 and Thr48 in MazF from *B. subtilis* and as Arg29 and Thr52 in MazF from *E. coli*. In MazF from *B. subtilis*, Arg25 is predicted to stabilize the cleavage of the P-O bond (46). In MazF from *E. coli*, Arg29 acts as both a general acid and general base, and Thr52 acts as a stabilizing residue (49). Our comparative analysis indicates that PemK from *S. aureus* may also be involved in mRNA cleavage mediated by acid-base catalysis of residues Arg25 and Thr48. Structural and functional studies on PemK from *S. aureus* revealed that Arg25 and Thr48 play a crucial role in PemK activity in addition to Arg84. It is hypothesized that Arg25 acts as both a general acid and base, and Thr48 stabilizes the transition state in the catalyzed reaction. This involvement of an Arg residue has been shown in other homologs, such as *E. coli* MazF and *B. subtilis* MazF (46,49). Interestingly, Arg84 was presented as a key residue in a previous study (17). Arg84 shows no direct interaction with ssRNA in our ssRNA-PemK complex model. However, the Arg84Ala mutant exhibited decreased RNase activity and RNA binding affinity. This essential role of Arg84 might originate from the involvement of hydrogen bonds in maintaining the ‘closed form’, which is catalytically optimal for RNA substrates.

As ribosome-independent RNases, PemK and its homologs recognize specific mRNA sequences. The most notable function of PemK is that it recognizes and cleaves specific tetrad mRNA sequences containing U↓AUU. The RNA sequence “UAUU” could be a codon or anticodon that may be further translated to Tyr or Ile. This selective degradation of transcripts and the subsequent growth inhibition demonstrate the toxicity of PemK in *S. aureus* (17). Inhibition of ribosomal-independent RNase activity of a toxin by its cognate antitoxin can be achieved by the formation of a TA complex, which thoroughly blocks mRNA binding by the toxin. According to the PemI-neutralized PemK structure, an α-helical toxin-binding motif of PemI causes conformational rearrangement of PemK from a ‘closed form’ to an ‘open form’ by binding to the active site residues.

In recent studies, structure-based small molecules or peptides designed to disrupt the toxin–antitoxin complexes and induce the artificial activation of toxin that results in cell death have been discovered (57–59). In addition to these strategies, an engineered toxin-intein was studied as an antimicrobial for the targeted killing of pathogens (60). Our study provides structural information on the toxin protein PemK that will enable researchers to discover inhibitors in the form of pseudopeptides or small molecules. The potential inhibitors could trigger perpetual toxin activation, leading to cell death of bacterial pathogens such as *S. aureus*.

DATA AVAILABILITY

Atomic coordinates and structure factors have been deposited into the Protein Data Bank (PDB) under the following accession codes: 7EWI for the PemK structure and 7EWJ for the PemIK structures, respectively.

SUPPLEMENTARY DATA

Supplementary Data are available at NAR Online.

ACKNOWLEDGEMENTS

We thank the staff members of the beamlines, PLS-5C of Pohang Accelerator Laboratory (Republic of Korea), AR-NW12A of Photon Factory (Japan) and BL44XU of SPring-8 (Japan) under the Collaborative Research Program of Institute for Protein Research, Osaka University (proposal no. 2019A6972) for assistance during X-ray diffraction experiments.

FUNDING

National Research Foundation of Korea (NRF) grant funded by the Korean government [2018R1A2A1A19018526 to B.-J.L., 2018R1A5A2024425 to B.-J.L., 2021R1F1A1050961 to B.-J.L., 2019R1C1C1002128 to S.-M.K., 2019R1I1A1A01057713 to D.-H.K., 2018R1A6B4023605 to S.J.L., 2020R1F1A1075828 to S.J.L.]; BK21 Plus Project for Medicine, Dentistry, and Pharmacy. Funding for open access charge: National Research Foundation of Korea.
Conflict of interest statement. None declared.

REFERENCES

1. Ogura,T. and Hiraga,S. (1983) Mini-F plasmid genes that couple host cell division to plasmid proliferation. *Proc. Natl. Acad. Sci. U.S.A.*, **80**, 4784–4788.
2. Holm,L. and Rosenstrom,P. (2010) Dali server: conservation mapping in 3D. *Nucleic Acids Res.*, **38**, W545–W549.
3. Yarmolinsky,M.B. (1995) Programmed cell death in bacterial populations. *Science*, **267**, 836–837.
4. Engelberg-Kulka,H., Amitai,S., Kolodkin-Gal,I. and Hazan,R. (2006) Bacterial programmed cell death and multicellular behavior in bacteria. *PLoS Genet.*, **2**, 1518–1526.
5. Yamaguchi,Y., Park,J.H. and Inouye,M. (2011) Toxin-antitoxin systems in bacteria and archaea. *Annu. Rev. Genet.*, **45**, 61–79.
6. Kang,S.M., Kim,D.H., Jin,C.L. and Lee,B.J. (2018) A systematic overview of type II and III toxin–antitoxin systems with a focus on druggability. *Toxins*, **10**, 515.
7. Page,R. and Peti,W. (2016) Toxin-antitoxin systems in bacterial growth arrest and persistence. *Nat. Chem. Biol.*, **12**, 208–214.
8. Cook,G.M., Robson,J.R., Frampton,R.A., McKenzie,J., Przybilski,R., Fineran,P.C. and Arcus,V.L. (2013) Ribonucleases in bacterial toxin–antitoxin systems. *Biochim.Biophys. Acta*, **1829**, 523–531.
9. Yamaguchi,Y. and Inouye,M. (2011) Regulation of growth and death in *Escherichia coli* by toxin–antitoxin systems. *Nat. Rev. Microbiol.*, **9**, 779–790.
10. Williams,J.J. and Hergenrother,P.J. (2012) Artificial activation of toxin–antitoxin systems as an antibacterial strategy. *Trends Microbiol.*, **20**, 291–298.
11. Pandey,D.P. and Gerdes,K. (2005) Toxin-antitoxin loci are highly abundant in free-living but lost from host-associated prokaryotes. *Nucleic Acids Res.*, **33**, 966–976.
12. Brown,J.M. and Shaw,K.J. (2003) A novel family of *Escherichia coli* toxin–antitoxin gene pairs. *J. Bacteriol.*, **185**, 6600–6608.
13. Schuster,C.F. and Bertram,R. (2016) Toxin-antitoxin systems of *Staphylococcus aureus*. *Toxins*, **8**, 140.
14. Zhu,L., Inoue,K., Yoshizumi,S., Kobayashi,H., Zhang,Y., Ouyang,M., Kato,F., Sugai,M. and Inouye,M. (2009) *Staphylococcus aureus* MazF specifically cleaves a pentad sequence, UACAU, which is unusually abundant in the mRNA for pathogenic adhesive factor SraP. *J. Bacteriol.*, **191**, 3248–3255.
15. Yoshizumi,S., Zhang,Y., Yamaguchi,Y., Chen,L., Kreiswirth,B.N. and Inouye,M. (2009) *Staphylococcus aureus* YoeB homologues inhibit translation initiation. *J. Bacteriol.*, **191**, 5868–5872.
16. Tsuchimoto,S., Ohtsubo,H. and Ohtsubo,E. (1988) Two genes, pemK and pemI, responsible for stable maintenance of resistance plasmid R100. *J. Bacteriol.*, **170**, 1461–1466.
17. Bukowski,M., Lyzen,R., Helbin,W.M., Bonar,E., Szalewska-Palasz,A., Wegrzyn,G., Dubin,G., Dubin,A. and Wladyka,B. (2013) A regulatory role for *Staphylococcus aureus* toxin–antitoxin system PemIKSa. *Nat. Commun.*, **4**, 2012.
18. Sengupta,M. and Austin,S. (2011) Prevalence and significance of plasmid maintenance functions in the virulence plasmids of pathogenic bacteria. *Infect. Immun.*, **79**, 2502–2509.
19. Nordstrom,K. and Austin,S.J. (1989) Mechanisms that contribute to the stable segregation of plasmids. *Annu. Rev.Genet.*, **23**, 37–69.
20. Zhang,J., Zhang,Y., Zhu,L., Suzuki,M. and Inouye,M. (2004) Interference of mRNA function by sequence-specific endoribonuclease PemK. *J. Biol. Chem.*, **279**, 20678–20684.
21. DeLeo,F.R., Diep,B.A. and Otto,M. (2009) Host defense and pathogenesis in *Staphylococcus aureus* infections. *Infect. Dis. Clin. North Am.*, **23**, 17–34.
22. Dreisbach,A., van Dijl,J.M. and Buist,G. (2011) The cell surface proteome of *Staphylococcus aureus*. *Proteomics*, **11**, 3154–3168.
23. Schlievert,P.M., Strandberg,K.L., Lin,Y.C., Peterson,M.L. and Leung,D.Y. (2010) Secreted virulence factor comparison between methicillin-resistant and methicillin-sensitive *Staphylococcus aureus*, and its relevance to atopic dermatitis. *J. Allergy Clin. Immunol.*, **125**, 39–49.
24. Torres,V.J., Attia,A.S., Mason,W.J., Hood,M.I., Corbin,B.D., Beasley,F.C., Anderson,K.L., Stauff,D.L., McDonald,W.H., Zimmerman,L.J. *et al.* (2010) *Staphylococcus aureus* fur regulates the expression of virulence factors that contribute to the pathogenesis of pneumonia. *Infect.Immun.*, **78**, 1618–1628.
25. Mir,D.A. and Balamurugan,K. (2019) Global proteomic response of *Caenorhabditis elegans* against PemKSa toxin. *Front. Cell Infect. Microbiol.*, **9**, 172.
26. Bleriot,I., Blasco,L., Delgado-Valverde,M., Gual de Torella,A., Ambroa,A., Fernandez-Garcia,L., Lopez,M., Oteo-Iglesias,J., Wood,T.K., Pascual,A. *et al.* (2020) Mechanisms of tolerance and resistance to chlorhexidine in clinical strains of *Klebsiella pneumoniae* producers of carbapenemase: role of new type II toxin-antitoxin system, PemIK. *Toxins*, **12**, 566.
27. Chi,X., Chang,Y., Li,M., Lin,J., Liu,Y., Li,C., Tang,S. and Zhang,J. (2018) Biochemical characterization of mt-PemIK, a novel toxin–antitoxin system in *Mycobacterium tuberculosis*. *FEBS lett.*, **592**, 4039–4050.
28. Bukowski,M., Hyz,K., Janczak,M., Hydzik,M., Dubin,G. and Wladyka,B. (2017) Identification of novel mazEF/pemIK family toxin–antitoxin loci and their distribution in the Staphylococcus genus. *Sci. Rep.*, **7**, 13462.
29. Takeuchi,S., Kinoshita,T., Kaidoh,T. and Hashizume,N. (1999) Purification and characterization of protease produced by *Staphylococcus aureus* isolated from a diseased chicken. *Vet. Microbiol.*, **67**, 195–202.
30. Otwinowski,Z. and Minor,W. (1997) Processing of X-ray diffraction data collected in oscillation mode. *Methods Enzymol.*, **276**, 307–326.
31. Kabsch,W. (2010) XDS. *Acta Crystallogr. Sect. D: Biol. Crystallogr.*, **66**, 125–132.
32. Mccoy,A.J., Grosse-Kunstleve,R.W., Adams,P.D., Winn,M.D., Storoni,L.C. and Read,R.J. (2007) Phaser crystallographic software. *J. Appl. Crystallogr.*, **40**, 658–674.
33. Hargreaves,D., Santos-Sierra,S., Giraldo,R., Sabariegos-Jareno,R., de la Cueva-Mendez,G., Boelens,R., Diaz-Orejas,R. and Rafferty,J.B. (2002) Structural and functional analysis of the kid toxin protein from *E. coli* plasmid R1. *Structure*, **10**, 1425–1433.
34. Adams,P.D., Afonine,P.V., Bunkoczi,G., Chen,V.B., Davis,I.W., Echols,N., Headd,J.J., Hung,L.W., Kapral,G.J., Grosse-Kunstleve,R.W. *et al.* (2010) PHENIX: a comprehensive Python-based system for macromolecular structure solution. *Acta Crystallogr. Sect. D: Biol. Crystallogr.*, **66**, 213–221.
35. Brunger,A.T. (1992) Free R value: a novel statistical quantity for assessing the accuracy of crystal structures. *Nature*, **355**, 472–475.
36. Emsley,P., Lohkamp,B., Scott,W.G. and Cowtan,K. (2010) Features and development of Coot. *Acta Crystallogr. Sect. D: Biol. Crystallogr.*, **66**, 486–501.
37. Murshudov,G.N., Vagin,A.A. and Dodson,E.J. (1997) Refinement of macromolecular structures by the maximum-likelihood method. *Acta Crystallogr. Sect. D: Biol. Crystallogr.*, **53**, 240–255.
38. Winn,M.D., Ballard,C.C., Cowtan,K.D., Dodson,E.J., Emsley,P., Evans,P.R., Keegan,R.M., Krissinel,E.B., Leslie,A.G., McCoy,A.

et al. (2011) Overview of the CCP4 suite and current developments. *Acta Crystallogr. Sect. D: Biol. Crystallogr.*, **67**, 235–242.
39. Chen,V.B., Arendall,W.B. 3rd, Headd,J.J., Keedy,D.A., Immormino,R.M., Kapral,G.J., Murray,L.W., Richardson,J.S. and Richardson,D.C. (2010) MolProbity: all-atom structure validation for macromolecular crystallography. *Acta Crystallogr. Sect. D: Biol. Crystallogr.*, **66**, 12–21.
40. Krissinel,E. and Henrick,K. (2007) Inference of macromolecular assemblies from crystalline state. *J. Mol. Biol.*, **372**, 774–797.
41. Tina,K.G., Bhadra,R. and Srinivasan,N. (2007) PIC: Protein Interactions Calculator. *Nucleic Acids Res.*, **35**, 473–476.
42. Delaglio,F., Grzesiek,S., Vuister,G.W., Zhu,G., Pfeifer,J. and Bax,A. (1995) NMRPipe: a multidimensional spectral processing system based on UNIX pipes. *J. Biomol. NMR*, **6**, 277–293.
43. Johnson,B.A. and Blevins,R.A. (1994) NMR View: A computer program for the visualization and analysis of NMR data. *J. Biomol. NMR*, **4**, 603–614.
44. Lundblad,J.R., Laurance,M. and Goodman,R.H. (1996) Fluorescence polarization analysis of protein-DNA and protein-protein interactions. *Mol. Endocrinol.*, **10**, 607–612.
45. van Zundert,G.C.P., Rodrigues,J., Trellet,M., Schmitz,C., Kastritis,P.L., Karaca,E., Melquiond,A.S.J., van Dijk,M., de Vries,S.J. and Bonvin,A. (2016) The HADDOCK2.2 web server: user-friendly integrative modeling of biomolecular complexes. *J. Mol. Biol.*, **428**, 720–725.
46. Simanshu,D.K., Yamaguchi,Y., Park,J.H., Inouye,M. and Patel,D.J. (2013) Structural basis of mRNA recognition and cleavage by toxin MazF and its regulation by antitoxin MazE in *Bacillus subtilis*. *Mol. Cell*, **52**, 447–458.
47. Abraham,M.J., Murtola,T., Schulz,R., Páll,S., Smith,J.C., Hess,B. and Lindahl,E. (2015) GROMACS: High performance molecular simulations through multi-level parallelism from laptops to supercomputers. *SoftwareX*, **1**, 19–25.
48. Valdes-Tresanco,M.S., Valdes-Tresanco,M.E., Valiente,P.A. and Moreno,E. (2021) gmx_MMPBSA: A new tool to perform end-state free energy calculations with GROMACS. *J. Chem. Theory Comput.*, **17**, 6281–6291.
49. Zorzini,V., Mernik,A., Lah,J., Sterckx,Y.G., De Jonge,N., Garcia-Pino,A., De Greve,H., Versees,W. and Loris,R. (2016) Substrate recognition and activity regulation of the *Escherichia coli* mRNA endonuclease MazF. *J. Biol. Chem.*, **291**, 10950–10960.
50. Zorzini,V., Buts,L., Sleutel,M., Garcia-Pino,A., Talavera,A., Haesaerts,S., De Greve,H., Cheung,A., van Nuland,N.A. and Loris,R. (2014) Structural and biophysical characterization of *Staphylococcus aureus* SaMazF shows conservation of functional dynamics. *Nucleic Acids Res.*, **42**, 6709–6725.
51. Verma,S., Kumar,S., Gupta,V.P., Gourinath,S., Bhatnagar,S. and Bhatnagar,R. (2014) Structural basis of *Bacillus anthracis* MoxXT disruption and the modulation of MoxT ribonuclease activity by rationally designed peptides. *J. Biomol. Struct. Dyn.*, **33**, 606–624.
52. Barbas,A., Matos,R.G., Amblar,M., Lopez-Vinas,E., Gomez-Puertas,P. and Arraiano,C.M. (2009) Determination of key residues for catalysis and RNA cleavage specificity: one mutation turns RNase II into a "SUPER-ENZYME". *J. Biol. Chem.*, **284**, 20486–20498.
53. Kamada,K., Hanaoka,F. and Burley,S.K. (2003) Crystal structure of the MazE/MazF complex: molecular bases of antidote-toxin recognition. *Mol.Cell*, **11**, 875–884.
54. Ahn,D.H., Lee,K.Y., Lee,S.J., Park,S.J., Yoon,H.J., Kim,S.J. and Lee,B.J. (2017) Structural analyses of the MazEF4 toxin–antitoxin pair in *Mycobacterium tuberculosis* provide evidence for a unique extracellular death factor. *J. Biol. Chem.*, **292**, 18832–18847.
55. Agarwal,S., Mishra,N.K., Bhatnagar,S. and Bhatnagar,R. (2010) PemK toxin of *Bacillus anthracis* is a ribonuclease: an insight into its active site, structure, and function. *J. Biol. Chem.*, **285**, 7254–7270.
56. Kamphuis,M.B., Bonvin,A.M., Monti,M.C., Lemonnier,M., Munoz-Gomez,A., van den Heuvel,R.H., Diaz-Orejas,R. and Boelens,R. (2006) Model for RNA binding and the catalytic site of the RNase Kid of the bacterial parD toxin–antitoxin system. *J.Mol.Biol.*, **357**, 115–126.
57. Kang,S.M., Jin,C., Kim,D.H., Lee,Y. and Lee,B.J. (2020) Structural and functional study of the *Klebsiella pneumoniae* VapBC toxin–antitoxin system, including the development of an inhibitor that activates VapC. *J. Med. Chem.*, **63**, 13669–13679.
58. Kang,S.M., Jin,C., Kim,D.H., Park,S.J., Han,S.W. and Lee,B.J. (2021) Structure-based design of peptides that trigger *Streptococcus pneumoniae* cell death. *FEBS J.*, **288**, 1546–1564.
59. Kang,S.M., Moon,H., Han,S.W., Kim,B.W., Kim,D.H., Kim,B.M. and Lee,B.J. (2021) Toxin-activating stapled peptides discovered by structural analysis were identified as new therapeutic candidates that trigger antibacterial activity against Mycobacterium tuberculosis in the *Mycobacterium smegmatis* model. *Microorganisms*, **9**. 568.
60. López-Igual,R., Bernal-Bayard,J., Rodriguez-Paton,A., Ghigo,J.-M. and Mazel,D. (2019) Engineered toxin–intein antimicrobials can selectively target and kill antibiotic-resistant bacteria in mixed populations. *Nat. Biotechnol.*, **37**, 755–760.
61. Madeira,F., Park,Y.M., Lee,J., Buso,N., Gur,T., Madhusoodanan,N., Basutkar,P., Tivey,A.R.N., Potter,S.C., Finn,R.D. *et al.* (2019) The EMBL-EBI search and sequence analysis tools APIs in 2019. *Nucleic Acids Res.*, **47**, 636–641.
62. Robert,X. and Gouet,P. (2014) Deciphering key features in protein structures with the new ENDscript server. *Nucleic Acids Res.*, **42**, 320–324.